

Resolving the Temperature and Composition Dependence of Ion Conductivity for Yttria-Stabilized Zirconia from Machine Learning Simulation

Published as part of *The Journal of Physical Chemistry virtual special issue "Machine Learning in Physical Chemistry"*.

Shu-Hui Guan, Cheng Shang* and Zhi-Pan Liu*

Cite This: *J. Phys. Chem. C* 2020, 124, 15085–15093

Read Online

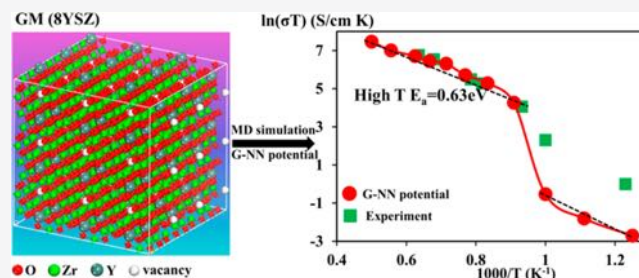
ACCESS |

Metrics & More

Article Recommendations

Supporting Information

ABSTRACT: The temperature and composition dependence of the ion conductivity for yttria-stabilized zirconia (YSZ) have been hotly studied over the past 50 years. Due to the sluggish oxygen anion diffusion and the low doping of oxide, the computation of ion conductivity traditionally has to be performed with empirical force field potentials in order to achieve the required long timescale, which, however, fails to reproduce some critical observations in experiment, e.g., the conductivity maximum achieved at 8 mol % YSZ at the operating temperatures. Here by using our recently developed Y–Zr–O global neural network (G-NN) potential, we are able to carry out a series of long-time molecular dynamics simulations for YSZ at 6.7, 8, 10, and 14.3 mol % over a wide temperature range (800–2000 K). This finally quantitatively resolves the effects of temperature and composition on the ion conductivity. We confirm the key experimental findings that (i) 8 mol % YSZ has the highest ion conductivity, 0.16–0.51 S/cm, at 1200–1600 K, agreeing with 0.16–0.55 S/cm in experiment, and the maximum conductivity shifts to the higher Y composition above 1600 K and (ii) over the wide temperature range (800–2000 K) the ion conductivity of 8YSZ exhibits the non-Arrhenius behaviors with two different activation energies. The physical origin for these peculiar phenomena is revealed at the atomic level by analyzing the MD pathways. The presence of monoclinic phase and the aggregation of oxygen vacancy along $\langle 112 \rangle$ are two key factors to retard oxygen diffusion. For 8 mol % YSZ, the oxygen movement is dominated by local vibrations below 1000 K but becomes delocalized above 1000 K, which results in the gradual aggregation of oxygen vacancy along a new $\langle 112 \rangle$ direction. Our results demonstrate that the G-NN potential from unbiased machine learning of the global potential energy surface can meet the high standard in both accuracy and speed required for material simulation.



1. INTRODUCTION

Yttria-stabilized zirconia (YSZ, $Y_{2x}Zr_{1-2x}O_{2-x}$) is one of the most important ion conducting solids, widely used in solid oxide fuel cells (SOFCs), solid oxide electrolysis cells (SOECs), and oxygen sensors.^{1–6} Chemically, the ion conduction in YSZ can be understood as the consequence of the motion of oxygen vacancies (O_v) that are present due to the charge balance required by doped Y^{3+} cations to replace Zr^{4+} . The ever-increasing observations on the measured conductivity from experiments are, however, far more intriguing than one's expectation. To name two of key significance: (i) the ion conductivity peaks at a particular low Y–Zr ratio^{7–11} at the operating temperatures (below 1670 K), i.e., 8 mol % Y_2O_3 (8YSZ) with typically 0.1–0.2 S/cm at 1273 °C,¹² but not at those with higher Y concentration and stoichiometrically more O_v ; (ii) while the conductivity increases with the lift of temperature, the high temperature and the low temperature regions exhibit distinct activation

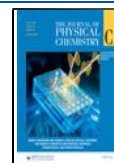
energies (E_a) according to the Arrhenius plot.^{13–17} The high temperature (>1073 K) barrier in 8YSZ is 0.70 eV^{12,17} but increases to 0.96–1.16 eV in 8YSZ at low temperatures (<973 K).^{16,18} Because of the difficulties in determining atom position and tracing atom motion in solid from experiment, it remains largely unclear on how O anions transport in YSZ.

Theoretical simulations have been the major tool in the field to understand the conductivity phenomena at the atomic level, mainly using molecular dynamics (MD) based on empirical force field potentials (e.g., in the form of Born–Mayer–

Received: May 14, 2020

Revised: June 18, 2020

Published: June 22, 2020



Huggins (BMH) potential^{19,20}). This situation is certainly a compromise because the low doping YSZ (e.g., 8YSZ) involves large cells in modeling and the slow oxygen transportation asks for long-time simulation. It has been well documented that, in contradiction to experiment, the computed diffusion coefficient reaches the maximum generally below 8 mol % Y_2O_3 below 1700 K (e.g., 6–8 mol % below 1125 K by Devanathan;²¹ 4 mol % below 1500 K by Araki;²² 6.4 mol % at 1250 K by Marrocchelli;²³ 7 mol % at 1273 K by Chang;²⁴ 5–7 mol % below 1700 K by Sizov;²⁵ 4–6 mol % below 1600 K by Huang;²⁶ more summarized in Table S1). As for the temperature dependence of conductivity, again few simulations can reproduce the experimental phenomena. Ngai et al.^{27,28} and Li et al.²⁹ proposed that the observed non-Arrhenius dependence of the conductivity was due to the glassy nature^{27–31} for 8YSZ using Vogel–Fulcher–Tammann law.³⁰ The barrier reduction from low to high temperature has been tentatively explained by many groups^{7,13,16,32,33} as the consequence of, for example, the likely $Y-O_v$ pairing below 900 K that constrains the motion of O_v , and the effect of the grain boundary on conductivity at low temperatures.^{18,34} These, however, were not evidenced directly by simulations. The above puzzles between theory and experiment may be attributed to two factors: (i) the inaccuracy of the force field potentials, which has been known to yield a wrong energy ordering of low energy structures as benchmarked against density functional theory (DFT) calculations.^{35,36} (ii) the uncertainty on the exact YSZ structures in experiment, including the phase (monoclinic, cubic, tetragonal), the Y (Zr) cation distribution, the defect, and phase boundaries. Considering that the Y distribution in YSZ was long believed to influence strongly the O_v diffusion, it is essential to determine that in stable structures of YSZ *in priori*, which was, however, not feasible using MD-based techniques based on force fields. The previous simulations generally assume the fluorite cubic crystal structure and utilize the random Y/Zr/ O_v distributions in cubic lattice as the initial configuration.

To solve the above puzzles, we recently developed the first machine learning potential for the Y–Zr–O ternary system, i.e., the YZrO global neural network (G-NN) potential,³⁶ which was validated by DFT calculations. Using stochastic surface walking^{37,38} global optimization based on G-NN potential (SSW-NN),^{39–41} we have identified the atomic structure for the most stable phase, the so-called global minimum (GM), for a series of YSZ with different Y concentrations, and thus established the thermodynamic convex hull diagram for YSZ. Fundamental knowledge on the atomic structure was thus established; for example, the pairing of Y cations with a Y–O–Y pattern is quite common in the GM of YSZ; O_v prefers to locate the nearby Zr cation as the first nearest neighbor (1NN) in general and align along particular crystallographic directions.³⁶

In this work, we continue our efforts to determine quantitatively the O anion transportation kinetics at elevated temperatures using machine learning simulation. Differently from previous work, we are now at a better position: first, equipping with a reliable Y–Zr–O G-NN potential; second, having a good knowledge on the GM structures and thus their cation positions. By performing extensive MD simulations for YSZ systems from 6.7YSZ to 14.3YSZ that are most relevant to engineering applications over a wide temperature range (800–2000 K), we obtain their ion conductivity and identify the oxygen diffusion pathways. In general, the machine learning

simulation results are quantitatively consistent with the known experimental data. The physical origin of the non-Arrhenius behavior is resolved by analyzing the O_v motion trajectory at different temperatures.

2. METHODS

All simulations based on G-NN potential were carried out by using our recently developed LASP code, Large-scale Atomic Simulation with neural network Potential (released at www.lasphub.com),⁴² which implements the data generation using SSW global optimization,^{37,38} training, and evaluation of G-NN potentials.³⁹ The Y–Zr–O ternary G-NN potential was trained by learning the global potential energy surface (PES) data generated by SSW global optimization, as reported previously.³⁶ In brief, the Y–Zr–O global data set consists of 28 803 structures, covering pure Zr, ZrO_x , Y_2O_3 , and Y/Zr ~ 1:9 to ~4:3 mixed oxides, that were calculated by plane-wave DFT calculations⁴³ at the high accuracy setup. The G-NN potential has a five-layer (188–60–50–50–1) feed-forward NN structure, in total 71 103 fitting parameters. The root-mean-square (RMS) errors for the energy and the force of the G-NN are 7.674 meV/atom and 0.165 eV/Å, respectively, for the global data set.

In order to identify the equilibrated volume (lattice), the initial structure relaxation was always carried out for 1 ns using the isothermal–isobaric (NPT) ensemble at the target temperature for YSZ systems at different Y concentrations. The ion motion was then simulated by using a Nose–Hoover thermostat^{44,45} at the canonic ensemble for YSZ systems ranging from 282 to 2528 atoms per supercell. Thanks to the high speed of G-NN potential calculations (>4 orders of magnitude faster than DFT calculations⁴⁶), we are able to carry out the long-time MD simulation for these large systems up to 10 ns with a time step of 1 fs. The first 1 ns of the NVT simulation was assigned to equilibrate the system and the statistic average of the anion diffusion was calculated over the remaining time. For the purpose of analysis, the local relaxation was utilized to obtain the intrinsic structure for the structure snapshots taken from MD trajectories until the maximal force on atom below 0.01 eV/Å.

The terms that are utilized and computed in this work are introduced as follows. The average radial distribution functions (RDF), $g(r)$, for Zr– O_v , Y– O_v , and O_v – O_v pairs can be computed using eq 1,

$$g_{X-O_v}(r) = \frac{V}{N_{O/O_v}} \frac{1}{N_X} \sum_{i=1}^{N_X} n_{O_v,i} \quad (1)$$

where the X represents the centering Zr, Y, or O_v ; $n_{O_v,i}$ is the number of O_v situated between the distance r to $r + \Delta r$ from the centering X atom. $g(r)$ is normalized by dividing the total number of centering atoms in the cell, the number of anionic sites N_{O/O_v} in the perfect cubic lattice ($=N_o + N_{O_v}$), and the volume of the cell (V). In the fluorite (cubic) structure, each O should be surrounded by four cations, i.e., at the center of a tetrahedron. The O_v analysis is thus basically to identify all tetrahedra formed by cations, each containing either one anion or one vacancy. To compute the RDF related to O_v , the vacancy coordinate can be determined by calculating the average value of the four nearby cations' coordinates.

The Einstein relation was used to determine the oxygen diffusion coefficients (D) from the slopes of mean square

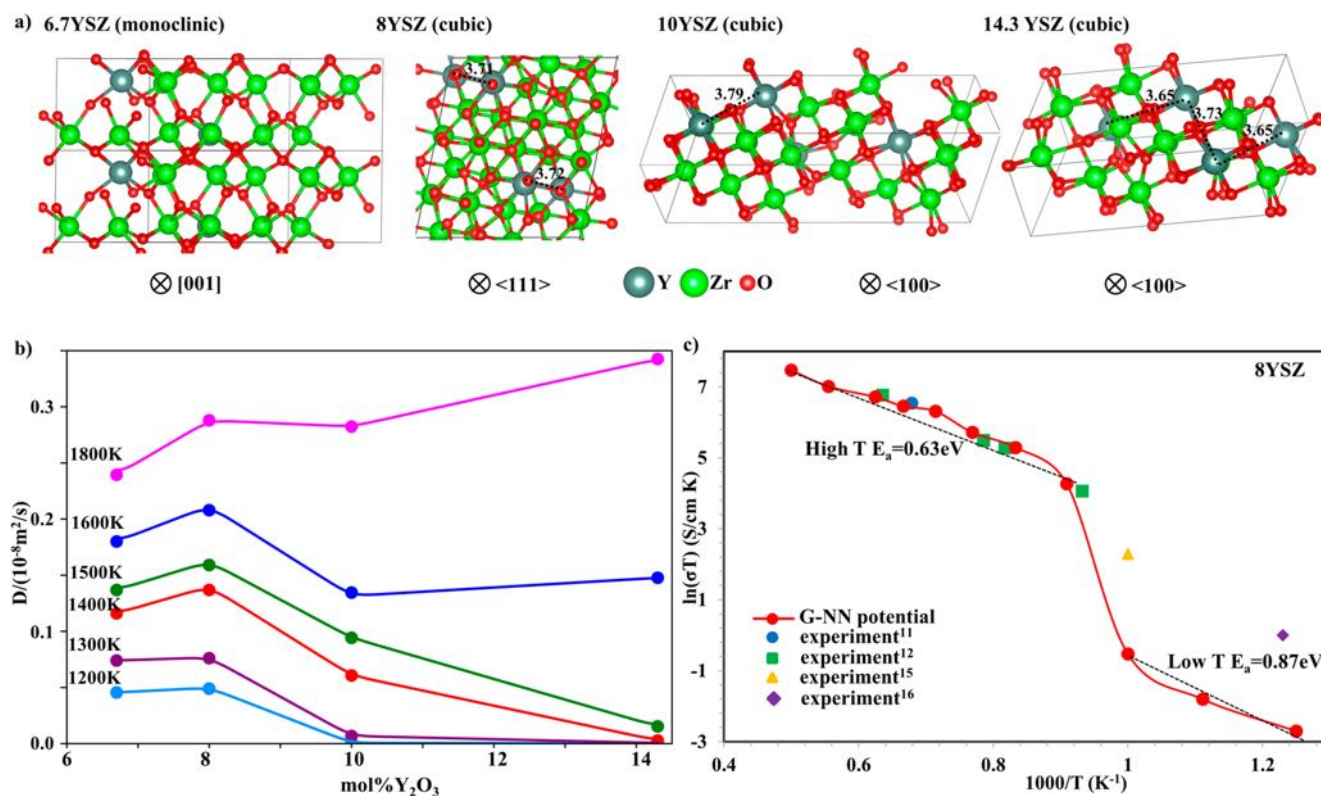


Figure 1. (a) GM structures of four YSZ systems determined in our previous work.³⁶ Important Y–Y distances are labeled in Å. (b) Oxygen diffusion coefficient D of oxygen vs the concentration of Y_2O_3 at different temperatures. (c) Arrhenius plot of the conductivity σ of 8YSZ with respect to temperature from 800 to 2000 K. The activation energies are obtained from the slope of the linear fitting applied to low and high temperature ranges as indicated in the figure.

displacements of oxygen atom (Δr^2) plotted versus simulation time (t):

$$D = \lim_{t \rightarrow \infty} \frac{\langle \Delta r(t)^2 \rangle}{6t} \quad (2)$$

The activation energies for oxygen diffusion (E_a) were computed by fitting the calculated diffusion coefficients to the standard Arrhenius form using the following relation:

$$D = D_0 \exp\left(-\frac{E_a}{RT}\right) \quad (3)$$

The E_a values thereby obtained were used to characterize the dependence of averaged diffusion barriers on different YSZ compositions. The conductivity of oxygen ions σ was finally derived from the Nernst–Einstein relation with the diffusion coefficient D :

$$\sigma = \frac{q^2 D N}{V N_a} \left(\frac{F^2}{RT}\right) \quad (4)$$

where N_a is the Avogadro constant, q is the charge of the mobile ion (2 for oxygen), N is the number of oxygen atoms, and F is the Faraday's constant.

3. RESULTS AND DISCUSSIONS

Models and Structures. Instead of using random cation distribution, our MD simulations start from the GM structures of $\text{Y}_{2x}\text{Zr}_{1-2x}\text{O}_{2-x}$ obtained in our recent work,³⁶ which have been confirmed by DFT calculations. Four low Y concentrations ($\text{Y}_2\text{O}_3\% = \text{Y}_2\text{O}_3/(\text{Y}_2\text{O}_3 + \text{ZrO}_2) = x/(1-x) = 6.7,$

8.0, 10.0, and 14.3 mol %) are chosen to understand the peculiar conductivity at 8YSZ. For convenience, these GM structures are also shown in Figure 1a and briefly introduced below.

We have found that, except for the GM of the lowest concentration, 6.7YSZ, that adopts the monoclinic lattice, the other three concentrations (8YSZ, 10YSZ, and 14.3YSZ) have the cubic phase GM. These results on the phase of GM are consistent with the phase diagram (at ambient temperature) reported in experiment.⁴⁷ With the increase of temperature, the monoclinic phase may transform to tetragonal/cubic phases (also see results below). It should be emphasized that in these GMs, the positions of Y cations are not random (see ref 36 for details). For example, in 8YSZ, every two Y cations tend to form pairs, in a Y–O–Y local pattern. The empirical force field potentials predict wrongly the GM where unpaired Y cations are preferred.

Ionic Conductivity. By performing long-time MD simulation using LASP, we have obtained the anion diffusion coefficient for the four YSZ samples within 400 atoms per cell, i.e., 6.7YSZ: $\text{Y}_{12}\text{Zr}_{84}\text{O}_{196}$, 8YSZ: $\text{Y}_{16}\text{Zr}_{92}\text{O}_{208}$, 10YSZ: $\text{Y}_{24}\text{Zr}_{108}\text{O}_{252}$, and 14.3YSZ: $\text{Y}_{32}\text{Zr}_{96}\text{O}_{240}$. In order to check the supercell size effect on the diffusion constant, the systems with more than 2000 atoms per cell were also performed at 1400 K. It shows that the diffusion coefficients obtained from the larger system is similar to the results obtained from the smaller cell (e.g., for 8YSZ at 1400 K the difference is $0.003 \times 10^{-8} \text{ m}^2/\text{s}$). Therefore, the oxygen diffusion coefficients reported here were calculated from the simulations within 400 atoms. This allows us to fast compute every YSZ composition for up to eight different temperatures with a

long timescale up to 10 ns. Typically, a few nanoseconds are found to be long enough to converge diffusion coefficient D at the operating conditions (example shown in the Figure S1).

The calculated diffusion coefficient D is plotted against the concentration of Y in Figure 1b from 1200 to 1800 K. For the first time, we show by simulation that the D of the oxygen anion peaks correctly at 8YSZ for a wide temperature range below 1600 K, reproducing the key finding in experiments.¹² With the increase of temperature to 2000 K, the maximum of the D curve shifts from 8 mol % to the higher dopant concentrations. This trend was also noticed by Nakamura et al.⁵¹ and Weller et al.⁵² in experiment (the temperature higher than 1600 K is out of the operation temperature of YSZ). Two important findings can be gleaned from our simulations: (i) the cubic phase enhances significantly the conductivity; (ii) the cationic distribution is also important to the conductivity. They are elaborated below.

As we stated above, 6.7YSZ prefers the monoclinic lattice in the GM. In simulation, we observe that 6.7YSZ remains as the monoclinic phase below 900 K, which could be distinguishable from simulated XRD pattern with the major peaks (2θ) at 28.1° and 30.1°, and the calculated D value is 60% less than that of 8YSZ (see Figure S2). But, it does undergo the phase transition to the cubic phase above 1200 K and thus the D difference with 8YSZ is reduced to 9.6% only. For comparison, we also examined the D value for an even lower dopant concentration, 5.3YSZ at 1400 K, which remains mostly as the monoclinic phase. Our results show that the D value is 100 times smaller than that of 8YSZ at 1400 K.

In our simulation, we never observe the cationic movement for all compositions up to 2000 K. This is understandable since the cationic movement has a very high barrier, ~ 5 eV.^{53,54} Because we adopt the cationic distribution as the GM, it is natural to wonder whether it is the random cationic distribution utilized previously by empirical force field calculations that shifts the conductivity peak to lower Y concentrations. Indeed, by using the same initial structure and BMH potential, we have repeated the same MD simulations as we did using the G-NN potential, and the results are shown in Figure S3. We found that, interestingly, the 8YSZ is still the peak composition with the BMH (Brinkman) potential,¹⁹ which confirms the importance for the correct cationic distribution on the conductivity. By comparing the results from G-NN (experiment) with those from BMH potential, we can see that the major difference occurs at the 6.7YSZ, where the force field predicts much too low D . Again, this should be caused by the lack of the natural phase transition from monoclinic to cubic due to the poor description of monoclinic phase by the force field.

Activation Energy. Our calculated conductivity σ values (using eq 4) for 8YSZ at different temperatures are shown in Figure 1c, and the available experimental data are also plotted in the figure for comparison. It can be seen that both theory and experiment show the transition of conductivity at ~ 1000 K, although the theoretical one appears to be much more abrupt (discussed below). At the operating temperature of YSZ, i.e., from 1200 to 1600 K, the simulated conductivity of 8YSZ ranges from 0.16 to 0.51 S/cm, well consistent with the experimental results^{11,12} from 0.16 to 0.55 S/cm. As listed in Table 1, the agreements between theory and experiment are also good for the other dopant concentrations at these temperatures. However, at the low temperatures, i.e., below 1000 K, the calculated data from theory are orders of

Table 1. Comparison of Selected Calculated Oxygen Conductivity in This Work with G-NN Potential, the Calculated Values from the Literature, and the Available Experiment Data

PES method	composition	T (K)	σ (S/cm)
G-NN potential (this work)	6.7YSZ	1600	0.44
	8YSZ	1200	0.16
		1300	0.23
		1500	0.42
	10YSZ	1600	0.51
		1600	0.32
1600		0.35	
BMH (Brinkman) ⁴⁸	8YSZ	1200	0.26
	1600	0.34	
		0.26	
BMH (modified Brinkman) ²⁶	8YSZ	1200	0.16
	1400	0.28	
		1600	0.39
BMH (Schelling) ²⁵	10YSZ	1600	0.33
	8YSZ	1300	0.11
		1500	0.18
BMH (Brinkman) ²⁵	8YSZ	1300	0.28
		1500	0.31
BMH (refitted) ⁴⁹	8.1YSZ	1500	0.13
	9.9YSZ	1500	0.49
	experiment	6.7YSZ ⁵⁰	1670
8YSZ ¹¹		1223	0.16
8YSZ ¹²		1273	0.19
8YSZ ¹²		1473	0.47
8YSZ ¹²		1573	0.55
10YSZ ¹²		1573	0.50
14.3YSZ ⁵⁰	1670	0.30	

magnitude lower than the experimental data. This may not be surprising since the diffusion of oxygen becomes extremely low in the perfect bulk (10^{-12} m²/s or smaller) below 1000 K and even a small amount of defect sites (e.g., phase boundaries) in the real material may become overwhelmingly important to the conductivity. In fact, this result is not new as the empirical potential calculations also find the low conductivity at the low temperatures.²⁵

By using the Arrhenius plot to correlate the conductivity σ with temperature, we have determined the activation energy E_a of anion diffusion for 8YSZ from the slope of the linear fit according to eq 3. Clearly, our data can only be approximated by two linear-fitted lines, one at high temperatures above 1000 K and one at low temperatures below 1000 K. From the fitted line, E_a is 0.63 eV above 1100 K and is 0.87 eV below 1000 K. These data compare well with the experimental data, i.e., 0.70 and 0.96–1.16 eV for the high and low temperature regions. Similarly, we also analyzed the Arrhenius behavior for 10YSZ and 14.3YSZ and found that all of them exhibit the temperature dependence of E_a . The high temperature and the low temperature E_a are 0.84 and 1.21 eV for 10YSZ, while it is 1.05 and 1.73 eV for 14.3YSZ.

It should be noted that E_a fitted from an Arrhenius plot may suffer from a certain uncertainty, in particular, at the low temperature region (< 1000 K) due to the slow convergence of the diffusion coefficient D . For example, 23% decrease in conductivity in 800 K may lead to the increase of E_a to 0.96 eV (increase 12%). We do observe that the D at 800 K has a high difficulty in convergence: even with a long simulation, 10 ns,

the value still oscillate by $\pm 25\%$. Nevertheless, because of the too low conductivity from the perfect bulk calculations that is beyond the numerical uncertainty, we can conclude quite safely that the presence of defects should dominate the low temperature measurement in reality and leads to the apparent discrepancy in conductivity between theory and experiment at low temperatures.

For now, our simulations succeed in reproducing three key facts observed in experiments, namely, the existence of diffusion coefficient maximum at 8YSZ below 1600 K,¹² the temperature dependence of the conductivity maximum,⁵² and the temperature dependence of the activation energy.¹⁶ To provide deeper insights into the above observations, we need to further analyze the structure evolution with the change of temperature and composition.

Structure Evolution for Different YSZ at 1400 K. Since the conductivity of YSZ is related to O_v motion, we have first analyzed the evolution of O_v distribution during the MD simulation. To do so, the structure snapshots taken every 20 ps from MD trajectories are fully relaxed to quench to the local minima, the so-called “intrinsic structure”, from which the vacancy position based on the ideal cubic lattice can be identified (see our previous work³⁶). The RDF associated with O_v can then be calculated by averaging the structure snapshots obtained over the equilibrium time. In Figure 2, we show the

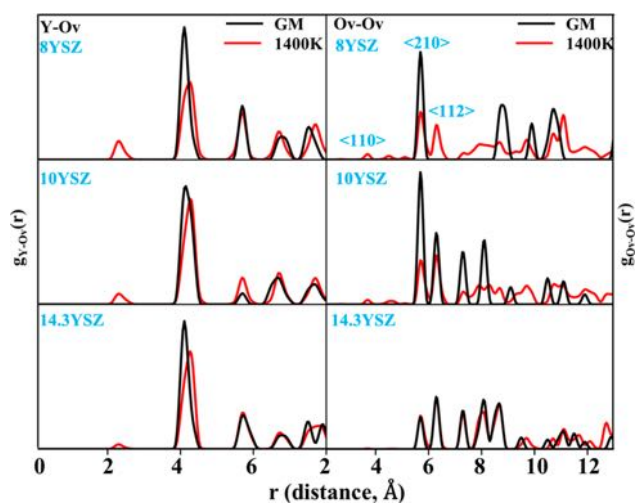


Figure 2. Radial distribution function $g(r)$ of the $Y-O_v$ (left panel) and O_v-O_v (right panel) pairs at 1400 K from MD simulation and those of the GM for 8YSZ, 10YSZ, and 14.3 YSZ.

$Y-O_v$ and O_v-O_v RDFs for 8YSZ, 10YSZ, and 14.3YSZ from MD trajectories at 1400 K (red lines), together with the same RDFs of the GM structures (black lines). The $Zr-O_v$ RDFs are shown in the Supporting Information in Figure S4 only since they are not sensitive to both the Y concentration of YSZ and temperature.

The RDFs of $Y-O_v$ shows that the $Y-O_v$ peaks appear at a series of characteristic positions for different YSZs, i.e., the first peak at ~ 2.3 Å, the second peak at ~ 4.1 Å, and so on. By comparing the RDFs at 1400 K with the RDF of GMs, we can see that the high temperature leads to the occurrence of $Y-O_v$ peaks at ~ 2.3 Å for all three YSZ compositions, indicating the O_v starts to populate at the first nearest neighbor (1NN) of Y, forming the $Y-O_v$ pattern. This is obviously caused by the oxygen migration. Considering the low intensity of the 1NN

peak, most O_v remain to locate near Zr. Furthermore, by comparing different YSZs, we find that the intensity of the first peak decreases with the increase of Y concentration from 8 to 14.3YSZ. This is in fact consistent with the O_v in 8YSZ having the highest diffusion coefficient and having the higher chance to appear near Y cations at 1400 K.

In line with the $Y-O_v$ RDFs, the O_v-O_v RDFs shown in the right panel of Figure 2 reflect clearly a more homogeneous distribution of O_v at 1400 K compared to those of GM, yielding a rather continuous curve in RDF. Two key features of O_v-O_v RDFs are summarized as follows.

(i) The close contact between O_v as reflected by the peaks related to the $\langle 100 \rangle$ (~ 2.5 Å) and $\langle 110 \rangle$ (~ 3.6 Å) directions are not favorable and only 8YSZ and 10YSZ show small peaks. Since O_v is generally near Zr, it suggests that the six-coordinated Zr with two O_v appearing in its 1NN shell, i.e., O_v-Zr-O_v , are indeed present, although with a low concentration, at the operating temperatures of YSZ.

(ii) The two peaks at the $\langle 210 \rangle$ (~ 5.8 Å) and $\langle 112 \rangle$ (~ 6.2 Å) directions form the primary feature in all three YSZ systems. For 8YSZ, the $\langle 210 \rangle$ peak remains as the highest peak, although the $\langle 112 \rangle$ peak is originally not present in the RDF for the GM of 8YSZ. By contrast, for 10YSZ and 14.3YSZ, the $\langle 112 \rangle$ peak is the highest. Since O_v tends to avoid O_v in oxygen diffusion, it is expected that the larger diffusion coefficient of 8YSZ arises from its preference of the $\langle 210 \rangle$ direction over the $\langle 112 \rangle$ direction. This is consistent with the knowledge obtained previously,³⁶ where the lowest energy pathway of oxygen diffusion in the GM is found to follow the $\langle 100 \rangle$ directions and thus has a chance (i.e., $[001]$) to avoid the nearby O_v when O_v is not present in the $\langle 112 \rangle$ direction.

In experiment, Kondoh et al.⁵⁵ by using extended X-ray absorption fine structure (EXAFS) observed the decrease in the 1NN coordination number of Zr ions (from 8 to 5.6) of 8YSZ at 1273 K for 1000 h. It suggests that the O_v aggregation near Zr occurs, i.e., O_v-Zr-O_v , in agreement with our results in O_v-O_v RDF. Goff et al.,⁵⁶ by using the neutron and X-ray diffraction, showed that the O_v preferentially arranges along the $\langle 111 \rangle$ direction below ~ 15 YSZ and, as the Y concentration increases, these $\langle 111 \rangle$ vacancy pairs pack together in $\langle 112 \rangle$ directions to form aggregates, which is detrimental to the conductivity. This finding also supports our results that the high intensity of the $\langle 112 \rangle$ peak would hinder the oxygen diffusion.

Structure Evolution of 8YSZ at Different Temperatures. Next, we focused on the structure evolution of 8YSZ at different temperatures in order to understand why the conductivity increases rapidly above 1000 K. Similarly, we have plotted in Figure 3 the $Y-O_v$ and O_v-O_v RDF for 8YSZ from 800 to 1400 K on the basis of the intrinsic structures from MD trajectories (the results above 1400 K are not particularly different from that at 1400 K and are shown in Figure S5).

The RDFs of $Y-O_v$ shows clearly the abrupt emergence of the peak at ~ 2.3 Å above 1000 K, where the $Y-O_v$ has the close contact. With the increase of temperature, this peak grows gradually in intensity, which is consistent with the increase of oxygen mobility at the higher temperatures. Except for the first peak, the temperature dependence of $Y-O_v$ RDF is not dramatic, only exhibiting the peak broadening at high temperatures.

For the RDF of O_v-O_v , similarly, they are largely the same as that of the GM when the temperature is below 1000 K. In parallel with the emergence of the new $Y-O_v$ peak at 2.3 Å

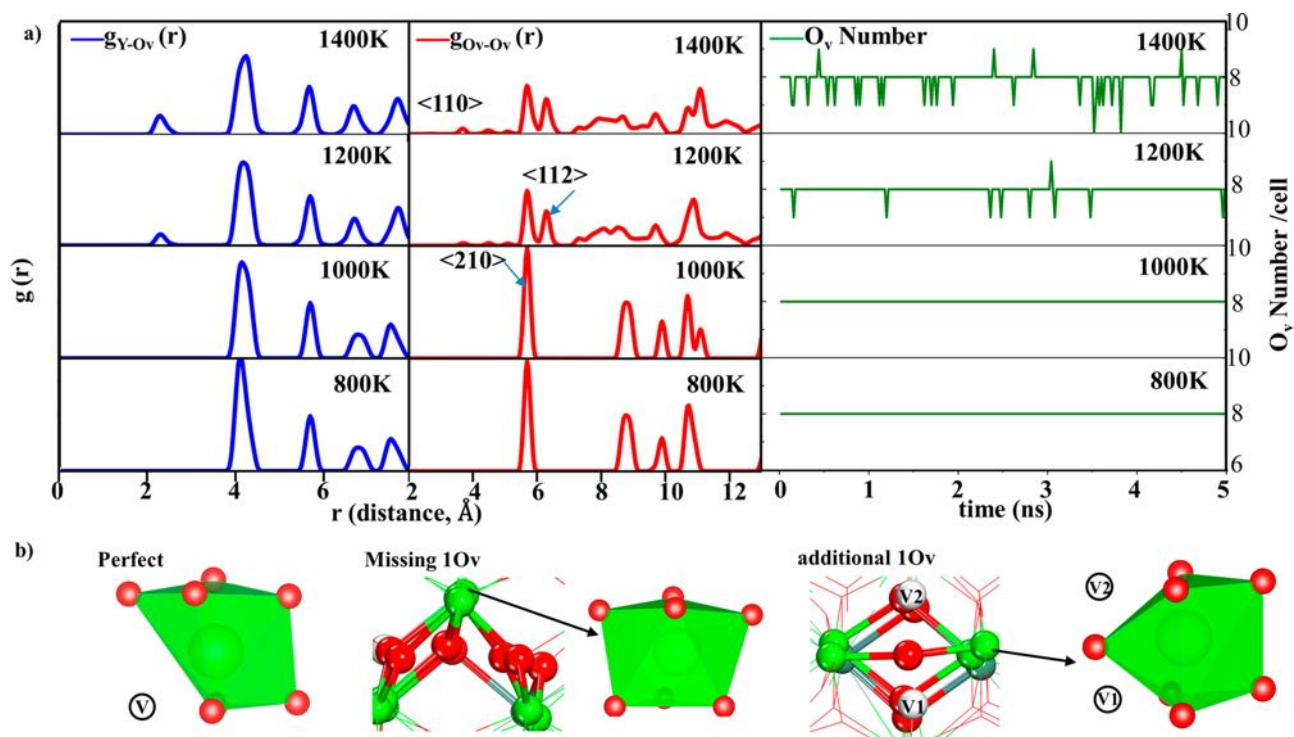


Figure 3. (a) Radial distribution function $g(r)$ of Y–O_v (left panel) and O_v–O_v (middle panel), and the apparent number of O_v in the intrinsic structure from MD trajectory (right panel) for 8YSZ at different temperatures. (b) Examples highlighting the local coordination pattern for a O_v in perfect cubic structure (left), the missing one O_v (middle) and the additional one O_v (right) identified in intrinsic structures from MD trajectory. All views are along the $\langle 110 \rangle$ direction.

above 1000 K, the O_v–O_v RDFs also experience a transition from 1000 to 1200 K: a new $\langle 112 \rangle$ peak appears in accompany with the shrinking of the $\langle 210 \rangle$ peak. In the meantime, the $\langle 110 \rangle$ peak (~ 3.6 Å) with the smallest separation between O_v starts to emerge at 1200 K, suggesting the tendency toward the homogeneous distribution for O_v above 1000 K.

In fact, due to the migration of O_v (oxygen anions) at high temperatures, the apparent number of O_v for the high-temperature structure snapshots along MD trajectory can oscillate, i.e., no longer constant as 8 per supercell, the stoichiometric number per Y₁₆Zr₉₂O₂₀₈ formula. Because the O_v can only be identified by matching with the perfect cubic lattice, the change of the O_v number implies the local distortion of the cubic structure obtained from MD simulations. As shown in the right panel of Figure 3a, we have plotted the variation of the apparent number of O_v with time. It is interesting to note that at low temperatures (800 and 1000 K), the apparent number of O_v is constant, being the nominal number 8. Above 1000 K, the number of O_v fluctuates and on average the number is below 8, specifically, decreasing from 7.97 at 1200 K to 7.88 at 1400 K, and finally to 7.14 at 2000 K.

To illustrate how the apparent O_v number oscillate, we have collected the local coordination patterns for the structures with unconventional O_v numbers in Figure 3b. The structure with one less O_v (missing 1Ov) is due to the oxygen anions movement along $[1\bar{1}0]$ direction: the two oxygen atoms near the original O_v position move along $[1\bar{1}0]$ direction that makes the original vacancy seemingly to disappear. By contrast, the structure with the O_v number increasing by one (additional 1O_v) is caused by one O atom moving along $\langle 001 \rangle$ direction by half O–O lattice length (~ 1.3 Å), producing two vacancies

(V1 and V2 in Figure 3b) near the central cation. Both phenomena stem from the local structural distortion away from the perfect cubic structure.

All these features confirm that O_v start to have a high mobility only above 1000 K. This is a consequence of the highly activated O migration: the high temperature contributes to the entropy gain and helps to overcome the high energy cost to move O_v away from their positions at the GM. It is thus expected that the two distinct apparent barriers in Figure 1c corresponding to the low and high temperatures are related to two different types of O_v motion: below 1000 K the lattice site vibration is dominated, while the long-range migration occurs above 1000 K. To confirm this, in the following we examine the pathways of oxygen motion at different temperatures.

Vacancy Migration Pathway. Finally, we inspected closely the MD trajectories for 8YSZ at 800 and 1400 K to understand how the O_v move at different temperatures. The structures every 100 fs from MD trajectories in a total 20 ps window were collected. By fully relaxing these structures to their intrinsic structures, we have obtained 31 reaction pairs for 800 K and 198 for 1400 K, where each reaction pair constitute two consecutive structures in MD trajectory, the initial (IS) and the final state (FS), but being different in their atom positions. Then, the reaction pathways between these reaction pairs were connected using double-ended surface walking (DESW) method,⁵⁷ and the transition states were located. In Figure 4, we show the reaction energy (the energy difference between FS and IS) versus the Euclidean distance (Å, the sum of the displacement of atoms) between the pair for the 800 and the 1400 K pathways.

We found that the reaction pairs at 800 K are generally close in geometry, distance below 2.2 Å, and the reaction energy is

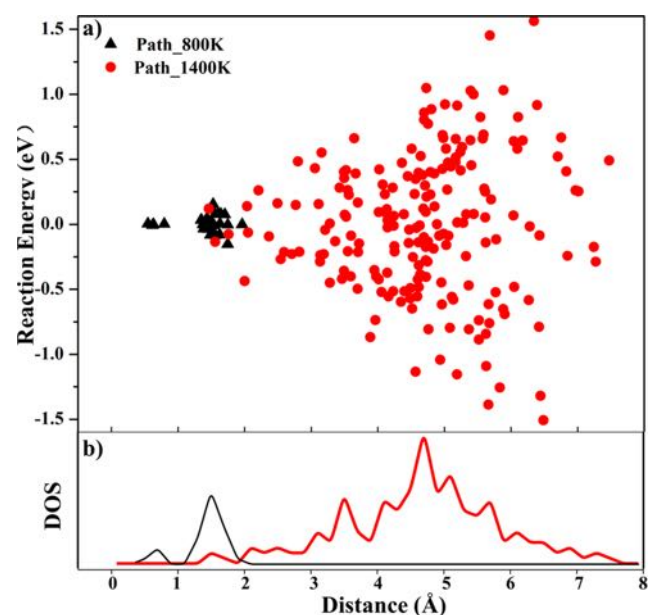


Figure 4. (a) Reaction pathways obtained from MD trajectories at 800 and 1400 K by plotting the reaction energy versus the Euclidean distances (the top panel). The reactions are those with structural changes in 100 fs by recording the two consecutive configurations from MD trajectories. (b) Density of the distances of the pathways.

generally lower than 0.4 eV in magnitude. Considering that the O_v diffusion to its 1NN position must involve an O atom diffusion of ~ 2.3 Å, there is essentially no O_v migration within 100 fs at 800 K but only the atomic vibration around their cubic lattice position. By contrast, at 1400 K, many reaction pathways have a long distance, up to 7.5 Å, as shown by the scattered red points in Figure 4a and the reaction energy can be as large as 1.6 eV in magnitude. The reactions with the distance ~ 4.7 Å are most populated, where the main peak occurs according to the calculated density of the states for the pathways (Figure 4b). These reactions can be different types, for example, a single O_v anion diffusion to its 3NN position along $\langle 111 \rangle$ direction (distance 4.4 Å) and a more than one O_v anion move to its 1NN position along $\langle 100 \rangle$ direction. In Figure S6, we illustrate such a reaction, where two O_v move within 100 fs, one jumping to its 2NN position along $\langle 110 \rangle$ and another to its 1NN position along $\langle 100 \rangle$. After the reaction, a Y– O_v pair forms at the FS and the reaction costs 1.09 eV. Since both IS and FS are the quenched intrinsic structure from the MD trajectory, it confirms that the large enthalpy cost due to the formation of Y– O_v pattern has been overcome by the entropy gain at 1400 K.

The above data explain that the measured activation energy for the ion conductivity at the operating temperature differ from that at the low temperature. The reaction switches from local vibration dominated movement to the long-range diffusion above 1000 K. The local nature of the oxygen movement at low temperatures is consistent with the very low ion conductivity calculated from theory, which in turn suggests that the experimental measured ion conductivity below 1000 K cannot be related to the bulk oxygen movement. At high temperatures, oxygen anions are no longer restrained to the lattice position, leading to intriguingly new features that are not present at low temperatures: (i) the formation of Y– O_v pairs; (ii) the increasing peak intensity at $\langle 112 \rangle$ direction; and (iii)

the oscillation of the apparent O_v number, leading to an apparent lower O_v population than that in stoichiometry.

4. CONCLUSION

With the advent of G-NN potential technique, this work revisits the ion conduction of YSZ at finite temperatures to understand the key puzzles in the field. Long-time MD simulations are carried out for four low doping YSZ systems up to 2000 K, starting from the GM configuration identified by us previously.³⁶ The simulated conductivity data reproduce quantitatively the key experimental findings, particularly, the highest conductivity achieved at 8YSZ below 1600 K. By analyzing the MD trajectories and the reaction pathways, we identify two factors that are critical to ion conductivity of YSZ: (i) the monoclinic phase that is the GM for YSZ with Y concentration less than 8 mol % can strongly hinder the oxygen diffusion; (ii) the O_v agglomeration along $\langle 112 \rangle$ that are typical for YSZ with Y concentration higher than 8 mol % retards the oxygen diffusion due to the strong O_v – O_v repulsion. These two factors are temperature- and composition-dependent and thus lead to intriguing phenomena observed in experiment, e.g., the maximum conductivity shifting to higher Y compositions above 1600 K and the non-Arrhenius behavior of conductivity around ~ 1000 K.

With the encouraging agreement between theory and experiment, this work demonstrates the great promise for future material simulation based on G-NN potentials as implemented in LASP (www.lasphub.com). This is because the current Y–Zr–O G-NN potential was established by learning the SSW global optimization data⁴⁶ that is from blind searches without any prior knowledge on the system, not by training limited high-temperature MD trajectories as done traditionally. With the good transferability, the high accuracy, and the high calculation speed provided by the G-NN potential, we believe that the G-NN potential can be an ideal alternative workhorse to reshape the simulation of large-size systems with a long timescale.

■ ASSOCIATED CONTENT

Supporting Information

The Supporting Information is available free of charge at <https://pubs.acs.org/doi/10.1021/acs.jpcc.0c04331>.


Summary of literature MD results for YSZ systems on the peak conductivity; diffusion coefficients vs simulation time; XRD patterns; oxygen diffusion coefficients vs concentration; RDFs of Zr– O_v pair for 8YSZ, 10YSZ, and 14.3YSZ at different temperatures; RDFs of cation– O_v and O_v – O_v for 8YSZ above 1600 K; selected O_v diffusion pathway of 8YSZ at 1400 K (PDF)

■ AUTHOR INFORMATION

Corresponding Authors

Cheng Shang – Collaborative Innovation Center of Chemistry for Energy Material, Shanghai Key Laboratory of Molecular Catalysis and Innovative Materials, Key Laboratory of Computational Physical Science, Department of Chemistry, Fudan University, Shanghai 200433, China; orcid.org/0000-0001-7486-1514; Email: cshang@fudan.edu.cn

Zhi-Pan Liu – Collaborative Innovation Center of Chemistry for Energy Material, Shanghai Key Laboratory of Molecular Catalysis and Innovative Materials, Key Laboratory of Computational Physical Science, Department of Chemistry,

Fudan University, Shanghai 200433, China;  orcid.org/0000-0002-2906-5217; Email: zpliu@fudan.edu.cn

Author

Shu-Hui Guan – Shanghai Academy of Agricultural Sciences, Shanghai 201403, China; Collaborative Innovation Center of Chemistry for Energy Material, Shanghai Key Laboratory of Molecular Catalysis and Innovative Materials, Key Laboratory of Computational Physical Science, Department of Chemistry, Fudan University, Shanghai 200433, China

Complete contact information is available at: <https://pubs.acs.org/10.1021/acs.jpcc.0c04331>

Notes

The authors declare no competing financial interest.

ACKNOWLEDGMENTS

This work was supported by the National Key Research and Development Program of China (2018YFA0208600) and the National Science Foundation of China (21533001 and 91745201).

REFERENCES

- (1) Steele, B. C.; Heinzl, A. Materials for Fuel-Cell Technologies. *Nature* **2001**, *414*, 345–352.
- (2) Ryskhewitch, E. Oxide ceramics: physical chemistry and technology. *Oxide ceramics: physical chemistry and technology*; Academic Press: New York, 1960; p 350.
- (3) Fabris, S.; Paxton, A. T.; Finnis, M. W. A stabilization mechanism of zirconia based on oxygen vacancies only. *Acta Mater.* **2002**, *50*, 5171–5178.
- (4) Chronos, A.; Yildiz, B.; Tarancón, A.; Parfitt, D.; Kilner, J. A. Oxygen diffusion in solid oxide fuel cell cathode and electrolyte materials: mechanistic insights from atomistic simulations. *Energy Environ. Sci.* **2011**, *4*, 2774–2789.
- (5) Garvie, R. C.; Hannink, R. H.; Pascoe, R. T. Ceramic steel? *Nature* **1975**, *258*, 703–704.
- (6) Jaipal, M.; Chatterjee, A. Relative Occurrence of Oxygen-Vacancy Pairs in Yttrium-Containing Environments of Y₂O₃-Doped ZrO₂. Can Be Crucial to Ionic Conductivity. *J. Phys. Chem. C* **2017**, *121*, 14534–14543.
- (7) Casselton, R. E. W. Low Field DC Conduction in Yttria-Stabilized Zirconia. *Phys. Status Solidi A* **1970**, *2*, 571–585.
- (8) Etsell, T. H.; Flengas, S. N. Electrical properties of solid oxide electrolytes. *Chem. Rev.* **1970**, *70*, 339–376.
- (9) Rühle, M. Microscopy of Structural Ceramics. *Adv. Mater.* **1997**, *9*, 195–217.
- (10) Yamamoto, O.; Arachi, Y.; Sakai, H.; Takeda, Y.; Imanishi, N.; Mizutani, Y.; Kawai, M.; Nakamura, Y. Zirconia Based Oxide Ion Conductors for Solid Oxide Fuel Cells. *Ionics* **1998**, *4*, 403–407.
- (11) Butz, B.; Kruse, P.; Stormer, H.; Gerthsen, D.; Müller, A.; Weber, A.; Iverstiffe, E. Correlation between microstructure and degradation in conductivity for cubic Y₂O₃-doped ZrO₂. *Solid State Ionics* **2006**, *177*, 3275–3284.
- (12) Kondoh, J.; Kawashima, T.; Kikuchi, S.; Tomii, Y.; Ito, Y. Effect of Aging on Yttria-Stabilized Zirconia I. A Study of Its Electrochemical Properties. *J. Electrochem. Soc.* **1998**, *145*, 1527–1536.
- (13) Guo, X.; Maier, J. Grain Boundary Blocking Effect in Zirconia: A Schottky Barrier Analysis. *J. Electrochem. Soc.* **2001**, *148*, E121.
- (14) Solier, J. d. D.; Perez-Jubindo, M. A.; Dominguez-Rodriguez, A.; Heuer, A. H. Low-Temperature Ionic Conductivity of 9.4-mol % Yttria Stabilized Zirconia Single Crystals. *J. Am. Ceram. Soc.* **1989**, *72*, 1500–1502.
- (15) Li, Y.; Gong, J. H.; Xie, Y. S.; Chen, Y. F. Analysis of non-linear Arrhenius behavior of ionic conduction in cubic zirconia stabilized with yttria and calcia. *J. Mater. Sci. Lett.* **2002**, *21*, 157–159.
- (16) Komine, S.; Munakata, F. Dielectric relaxation analysis for 8 mol% YSZ. single crystal. *J. Mater. Sci.* **2005**, *40*, 3887–3890.
- (17) Lakki, A.; Herzog, R.; Weller, M.; Schubert, H.; Reetz, C.; Görke, O.; Kilo, M.; Borchardt, G. Mechanical loss, creep, diffusion and ionic conductivity of ZrO₂-8 mol%Y₂O₃ polycrystals. *J. Eur. Ceram. Soc.* **2000**, *20*, 285–296.
- (18) De Souza, R. A.; Pietrowski, M. J.; Anselmi-Tamburini, U.; Kim, S.; Munir, Z. A.; Martin, M. Oxygen diffusion in nanocrystalline yttria-stabilized zirconia: the effect of grain boundaries. *Phys. Chem. Chem. Phys.* **2008**, *10*, 2067–2072.
- (19) Brinkman, H. W.; Briels, W. J.; Verweij, H. Molecular dynamics simulations of yttria-stabilized zirconia. *Chem. Phys. Lett.* **1995**, *247*, 386–390.
- (20) Dwivedi, A.; Cormack, A. N. A computer simulation study of the defect structure of calcia-stabilized zirconia. *Philos. Mag. A* **1990**, *61*, 1–22.
- (21) Devanathan, R.; Weber, W.; Singhal, S.; Gale, J. Computer simulation of defects and oxygen transport in yttria-stabilized zirconia. *Solid State Ionics* **2006**, *177*, 1251–1258.
- (22) Araki, W.; Arai, Y. Molecular dynamics study on oxygen diffusion in yttria-stabilized zirconia subjected to uniaxial stress in terms of yttria concentration and stress direction. *Solid State Ionics* **2010**, *181*, 1534–1541.
- (23) Marrocchelli, D.; Madden, P. A.; Norberg, S. T.; Hull, S. Structural Disorder in Doped Zirconias, Part II: Vacancy Ordering Effects and the Conductivity Maximum. *Chem. Mater.* **2011**, *23*, 1365–1373.
- (24) Chang, K. S.; Lin, Y. F.; Tung, K. L. Insight into the grain boundary effect on the ionic transport of yttria-stabilized zirconia at elevated temperatures from a molecular modeling perspective. *J. Power Sources* **2011**, *196*, 9322–9330.
- (25) Sizov, V. V.; Lampinen, M. J.; Laaksonen, A. Molecular dynamics simulation of oxygen diffusion in cubic yttria-stabilized zirconia: Effects of temperature and composition. *Solid State Ionics* **2014**, *266*, 29–35.
- (26) Huang, H. C.; Su, P. C.; Kwak, S. K.; Pornprasertsuk, R.; Yoon, Y. J. Molecular Dynamics Simulation of Oxygen Ion Diffusion in Yttria Stabilized Zirconia Single Crystals and Bicrystals. *Fuel Cells* **2014**, *14*, 574–580.
- (27) Ngai, K. L. Evidence of interaction between oxygen ions from conductivity relaxation and quasielastic light scattering data of yttria-stabilized zirconia. *Philos. Mag. B* **1998**, *77*, 187–195.
- (28) Ngai, K. L.; Greaves, G. N.; Moynihan, C. T. Correlation between the Activation Energies for Ionic Conductivity for Short and Long Time Scales and the Kohlrausch Stretching Parameter b for Ionically Conducting Solids and Melts. *Phys. Rev. Lett.* **1998**, *80*, 1019–1021.
- (29) Dong, Y.; Qi, L.; Li, J.; Chen, I. W. A computational study of yttria-stabilized zirconia: I. Using crystal chemistry to search for the ground state on a glassy energy landscape. *Acta Mater.* **2017**, *127*, 73–84.
- (30) Ribes, M.; Taillades, G.; Pradel, A. Non-Arrhenius conductivity in glassy and crystallized fast ion conductors, A manifestation of cationic disorder. *Solid State Ionics* **1998**, *105*, 159–165.
- (31) Habasaki, J.; León, C.; Ngai, K. L. Electrical Response of Ionic Conductors. *Top. Appl. Phys.* **2017**, *132*, 89–250.
- (32) Kilner, J. A.; Waters, C. D. The effects of dopant cation-oxygen vacancy complexes on the anion transport properties of non-stoichiometric fluorite oxides. *Solid State Ionics* **1982**, *6*, 253–259.
- (33) Nowick, A. S.; Park, D. S.; Mahen, G.; Roth, W. *Superionic Conductors*; Plenum Press: New York, 1976; p 395.
- (34) Durá, O. J.; López de la Torre, M. A.; Vázquez, L.; Chaboy, J.; Boada, R.; Rivera-Calzada, A.; Santamaria, J.; Leon, C. Ionic conductivity of nanocrystalline yttria-stabilized zirconia: Grain boundary and size effects. *Phys. Rev. B* **2010**, *81*, 184301.
- (35) Parkes, M. A.; Tompsett, D. A.; d’Avezac, M.; Offer, G. J.; Brandon, N. P.; Harrison, N. M. The atomistic structure of yttria stabilised zirconia at 6.7 mol%: an ab initio study. *Phys. Chem. Chem. Phys.* **2016**, *18*, 31277–31285.

- (36) Guan, S.-H.; Zhang, K.-X.; Shang, C.; Liu, Z.-P. Stability and anion diffusion kinetics of Ytria-stabilized zirconia resolved from machine learning global potential energy surface exploration. *J. Chem. Phys.* **2020**, *152*, 094703.
- (37) Shang, C.; Liu, Z.-P. Stochastic Surface Walking Method for Structure Prediction and Pathway Searching. *J. Chem. Theory Comput.* **2013**, *9*, 1838–1845.
- (38) Shang, C.; Zhang, X.-J.; Liu, Z.-P. Stochastic surface walking method for crystal structure and phase transition pathway prediction. *Phys. Chem. Chem. Phys.* **2014**, *16*, 17845–17856.
- (39) Huang, S.-D.; Shang, C.; Zhang, X.-J.; Liu, Z.-P. Material discovery by combining stochastic surface walking global optimization with a neural network. *Chem. Sci.* **2017**, *8*, 6327–6337.
- (40) Huang, S.-D.; Shang, C.; Kang, P.-L.; Liu, Z.-P. Atomic structure of boron resolved using machine learning and global sampling. *Chem. Sci.* **2018**, *9*, 8644–8655.
- (41) Ma, S.; Huang, S.-D.; Liu, Z.-P. Dynamic coordination of cations and catalytic selectivity on zinc-chromium oxide alloys during syngas conversion. *Nat. Catal.* **2019**, *2*, 671–677.
- (42) Huang, S.-D.; Shang, C.; Kang, P.-L.; Zhang, X.-J.; Liu, Z.-P. LASP: Fast global potential energy surface exploration. *Wiley Interdiscip. Rev.: Comput. Mol. Sci.* **2019**, No. e1415.
- (43) Kresse, G.; Furthmüller, J. Efficiency of ab-initio total energy calculations for metals and semiconductors using a plane-wave basis set. *Comput. Mater. Sci.* **1996**, *6*, 15–50.
- (44) Hoover, W. G. Canonical dynamics: Equilibrium phase-space distributions. *Phys. Rev. A: At., Mol., Opt. Phys.* **1985**, *31*, 1695–1697.
- (45) Nose, S. A unified formulation of the constant temperature molecular dynamics methods. *J. Chem. Phys.* **1984**, *81*, 511.
- (46) Huang, S. D.; Shang, C.; Zhang, X. J.; Liu, Z. P. Material discovery by combining stochastic surface walking global optimization with a neural network. *Chem. Sci.* **2017**, *8*, 6327–6337.
- (47) Suzuki, Y. Phase transition temperature of fluorite-type ZrO₂-Y₂O₃ solid solutions containing 8–44 mol% Y₂O₃. *Solid State Ionics* **1995**, *81*, 211–216.
- (48) Arima, T.; Fukuyo, K.; Idemitsu, K.; Inagaki, Y. Molecular dynamics simulation of yttria-stabilized zirconia between 300 and 2000 K. *J. Mol. Liq.* **2004**, *113*, 67–73.
- (49) Yang, C.; Trachenko, K.; Hull, S.; Todorov, I. T.; Dove, M. T. Emergence of microstructure and oxygen diffusion in yttrium-stabilized cubic zirconia. *Phys. Rev. B: Condens. Matter Mater. Phys.* **2018**, *97*, 184107.
- (50) Subbarao, E.; Ramakrishnan, T. Fast Ion Transport in Solids. *Fast Ion Transport in Solids*; Elsevier/North Holland: New York, 1979; pp 653–656.
- (51) Nakamura, A. J.; Bruce Wagner, J. Defect Structure, Ionic Conductivity, and Diffusion in Ytria Stabilized Zirconia and Related Oxide Electrolytes with Fluorite Structure. *J. Electrochem. Soc.* **1986**, *133*, 1542–1548.
- (52) Weller, M. Oxygen mobility in yttria-doped zirconia studied by internal friction, electrical conductivity and tracer diffusion experiments. *Solid State Ionics* **2004**, *175*, 409–413.
- (53) Chien, F. R.; Heuer, A. H. Lattice diffusion kinetics in Y₂O₃-stabilized cubic ZrO₂ single crystals: A dislocation loop annealing study. *Philos. Mag. A* **1996**, *73*, 681–697.
- (54) Kilo, M.; Borchardt, G.; Lesage, B.; Kaitasov, O.; Weber, S.; Scherrer, S. Cation transport in yttria stabilized cubic zirconia: ⁹⁶Zr tracer diffusion in (Zr_xY_{1-x})O_{1-2/x} single crystals with 0.15 ≤ x ≤ 0.48. *J. Eur. Ceram. Soc.* **2000**, *20*, 2069–2077.
- (55) Kondoh, J.; Kikuchi, S.; Tomii, Y.; Ito, Y. Effect of Aging on Ytria Stabilized Zirconia III. A Study of the Effect of Local Structures on Conductivity. *J. Electrochem. Soc.* **1998**, *145*, 1550–1560.
- (56) Goff, J. P.; Hayes, W.; Hull, S.; Hutchings, M. T.; Clausen, K. N. Defect structure of yttria-stabilized zirconia and its influence on the ionic conductivity at elevated temperatures. *Phys. Rev. B: Condens. Matter Mater. Phys.* **1999**, *59*, 14202–14219.
- (57) Zhang, X.-J.; Shang, C.; Liu, Z.-P. Double-Ended Surface Walking Method for Pathway Building and Transition State Location of Complex Reactions. *J. Chem. Theory Comput.* **2013**, *9*, 5745–5753.